Aberration-corrected scanning transmission electron microscopy: from atomic imaging and analysis to solving energy problems

S. J. Pennycook, M. F. Chisholm, A. R. Lupini, M. Varela, A. Y. Borisevich, M. P. Oxley, W. D. Luo, K. van Benthem, S.-H. Oh, D. L. Sales, S. I. Molina, J. García-Barriocanal, C. Leon, J. Santamaría, S. N. Rashkeev and S. T. Pantelides

Supplementary data	"Audio Supplement" http://rsta.royalsocietypublishing.org/content/suppl/2009/08/11/367.1903.3709.DC1.html
References	**This article cites 67 articles, 11 of which can be accessed free** http://rsta.royalsocietypublishing.org/content/367/1903/3709.full.html#ref-list-1
Subject collections	Articles on similar topics can be found in the following collections electron microscopy (18 articles)
Email alerting service	Receive free email alerts when new articles cite this article - sign up in the box at the top right-hand corner of the article or click **here**

REVIEW

Aberration-corrected scanning transmission electron microscopy: from atomic imaging and analysis to solving energy problems

BY S. J. PENNYCOOK[1,2,*], M. F. CHISHOLM[1], A. R. LUPINI[1], M. VARELA[1], A. Y. BORISEVICH[1], M. P. OXLEY[1,2], W. D. LUO[1,2], K. VAN BENTHEM[3], S.-H. OH[4], D. L. SALES[5], S. I. MOLINA[5], J. GARCíA-BARRIOCANAL[6], C. LEON[6], J. SANTAMARíA[6], S. N. RASHKEEV[7] AND S. T. PANTELIDES[1,2]

[1] *Materials Science and Technology Division, Oak Ridge National Laboratory, Oak Ridge, TN 37831, USA*
[2] *Department of Physics and Astronomy, Vanderbilt University, Nashville, TN 37235, USA*
[3] *Department of Chemical Engineering and Materials Science, University of California, Davis, CA 95616, USA*
[4] *Korea Basic Science Institute, Daejeon, Republic of Korea*
[5] *Departamento de Ciencia de los Materiales e I.M. y Q.I., Universidad de Cádiz, Spain*
[6] *GFMC, Universidad Complutense de Madrid, Madrid 28040, Spain*
[7] *Idaho National Laboratory, Idaho Falls, ID 83415, USA*

The new possibilities of aberration-corrected scanning transmission electron microscopy (STEM) extend far beyond the factor of 2 or more in lateral resolution that was the original motivation. The smaller probe also gives enhanced single atom sensitivity, both for imaging and for spectroscopy, enabling light elements to be detected in a Z-contrast image and giving much improved phase contrast imaging using the bright field detector with pixel-by-pixel correlation with the Z-contrast image. Furthermore, the increased probe-forming aperture brings significant depth sensitivity and the possibility of optical sectioning to extract information in three dimensions. This paper reviews these recent advances with reference to several applications of relevance to energy, the origin of the low-temperature catalytic activity of nanophase Au, the nucleation and growth of semiconducting nanowires, and the origin of the eight orders of magnitude increased ionic conductivity in oxide superlattices. Possible future directions of aberration-corrected STEM for solving energy problems are outlined.

*Author for correspondence (pennycooksj@ornl.gov).

1. Introduction

The successful implementation of aberration correction in the field of transmission electron microscopy (TEM) (Haider *et al.* 1998; Batson *et al.* 2002) has precipitated a rate of instrumental advance unparalleled since the 1930s. The benefits for scanning TEM (STEM) have arguably been greater than those for conventional TEM owing to the improvement in signal-to-noise ratio made possible by the availability of higher probe currents. For example, the record for image resolution, previously held exclusively by TEM, has moved to STEM, as seen by the direct imaging of the dumbbell in Si ⟨1 1 2⟩ at 0.78 Å, shown in figure 1 (Nellist *et al.* 2004), and more recently by the resolution of 0.63 Å in wurtzite GaN in the ⟨2 1 1⟩ projection (Sawada *et al.* 2007; Kisielowski *et al.* 2008) (see also figure 2). The detectability of individual atoms has improved markedly, whether on the surface of a material or inside the bulk; compare, for example, the images in Nellist & Pennycook (1996) and Voyles *et al.* (2002) with the aberration-corrected counterparts in Lupini & Pennycook (2003) and Sohlberg *et al.* (2004). We have seen the spectroscopic identification of a single atom (Varela *et al.* 2004) and two-dimensional spectrum imaging with good statistics (Bosman *et al.* 2007; Muller *et al.* 2008).

The larger probe-forming aperture made possible by aberration correction has also brought some unanticipated advantages. The reduced depth of field has brought the possibility of optical sectioning (van Benthem *et al.* 2005; Borisevich *et al.* 2006*a*,*b*; van Benthem *et al.* 2006; Marinopoulos *et al.* 2008) and even true confocal microscopy with double-corrected instruments (Nellist *et al.* 2006, 2008). Point defect configurations for heavy atoms can be determined inside materials (Oh *et al.* 2008; Roberts *et al.* 2008). Phase contrast imaging in STEM has also benefited dramatically from aberration correction, not just because of the larger available probe currents, but because the collector aperture can be opened up an order of magnitude while maintaining coherent imaging conditions (Pennycook 2006). Simultaneous incoherent high angle annular dark field (ADF), or Z-contrast imaging, and bright field phase contrast imaging provide two different channels of information about the specimen.

Another benefit of the clearer view available with aberration correction is the more accurate comparison of experiment with theory, whether it be dynamical diffraction theory for understanding issues such as beam broadening and localization in imaging and spectroscopy (Oxley *et al.* 2007; LeBeau *et al.* 2008; Oxley & Pennycook 2008; Peng *et al.* 2008) or density functional theory for understanding the atomic origin of materials properties. In both cases, the substantial advances in computational power over the last few years mean that systems requiring hundreds of atoms, such as grain boundaries or nanostructures, can now be tackled.

In this paper, we present some of these significant instrumental advances and then describe some recent applications to energy problems using a combination of microscopy and theory, specifically the origin of the remarkably high activity of gold nanocatalysts for the oxidation of CO to CO_2, detection of the nucleation sites for semiconductor nanowires and explanation of their subsequent morphological evolution and the investigation of oxide superlattices showing eight orders of magnitude enhanced oxygen ion conductivity, which suggests a route towards the realization of solid oxide low-temperature fuel cells. Finally, we

discuss possible future directions for investigating energy issues using the ability of the STEM to correlate imaging and spectroscopy with other signals generated by the probe. Cathodoluminescence detection would allow correlation of light emission with dislocation core structure and impurity segregation for solid-state lighting applications (Pennycook 2008), electron beam-induced conductivity (EBIC) could provide charge collection maps of solar cell materials and an *in situ* scanning tunnelling microscope could enable bias to be applied to local areas in materials to probe the effect of band bending and local electric fields.

Many of the results presented here have been previously published, and the original papers should be consulted for more details and additional references. Some of the material has also appeared in other review articles (Varela *et al.* 2005; Chisholm & Pennycook 2006; Pennycook *et al.* 2006, 2007, 2008*a*,*b*; Lupini *et al.* 2007).

2. New possibilities with aberration-corrected scanning transmission electron microscopy

Figure 1*a* shows the first direct image of a crystal lattice demonstrating sub-angstrom resolution, Si $\langle 1\,1\,2 \rangle$, obtained on the Oak Ridge National Laboratory (ORNL) VG Microscopes HB603U STEM. A clear dip in intensity is visible in the centre of every dumbbell, showing the resolution to be 0.78 Å (Nellist *et al.* 2004). Least-squares fitting to image simulations allowed the experimental parameters of thickness, defocus and incoherent broadening to be extracted (Peng *et al.* 2008). The zero-order spot was used as an adjustable parameter, to avoid issues with any background intensity or Stobbs factor. The best-fit image simulation is shown in figure 1*b*, whereas figure 1*c* shows a comparison between the experimental and best-fit theoretical intensity profiles. The coherent aberrations alone give a probe full-width half-maximum (FWHM) of 0.46 Å. The best-fit image simulation modelled the incoherent broadening as a 0.6 Å Gaussian, which when convolved with a probe gives an FWHM of 0.74 Å, resulting in a dip of 11 per cent between the two columns of the dumbbell. A resolution criterion of a 10 per cent dip was proposed, since all the dumbbells are seen to be resolved experimentally, and so the Rayleigh value of 27 per cent seems unnecessarily severe. Comparing the spot intensities in the Fourier transform (figure 1*d*) with the noise background revealed the information limit and associated confidence level. The $44\bar{4}$ spot, which corresponds to the dumbbell separation of 0.784 Å, gave a confidence level of 97 per cent, while the $08\bar{4}$ spot at 0.607 Å had a confidence level of 71 per cent representing the effective information cut-off.

Figure 2 shows the resolution of Ga dumbbells separated by 0.63 Å in a Z-contrast image of wurtzite GaN in the $\langle 2\,1\,1 \rangle$ orientation, obtained on the FEI Titan 80-300 aberration-corrected STEM at ORNL equipped with the CEOS DCOR aberration corrector (Müller *et al.* 2006) and a prototype FEI high brightness gun. With the DCOR, full correction of all third-, fourth- and fifth-order aberrations is achievable to a level that is theoretically sufficient to allow a probe size of 0.5 Å. The high brightness gun is still a thermally assisted Schottky-type gun that has brightness that is higher by about a factor of 4–5 over the standard gun. This microscope was installed as part of the
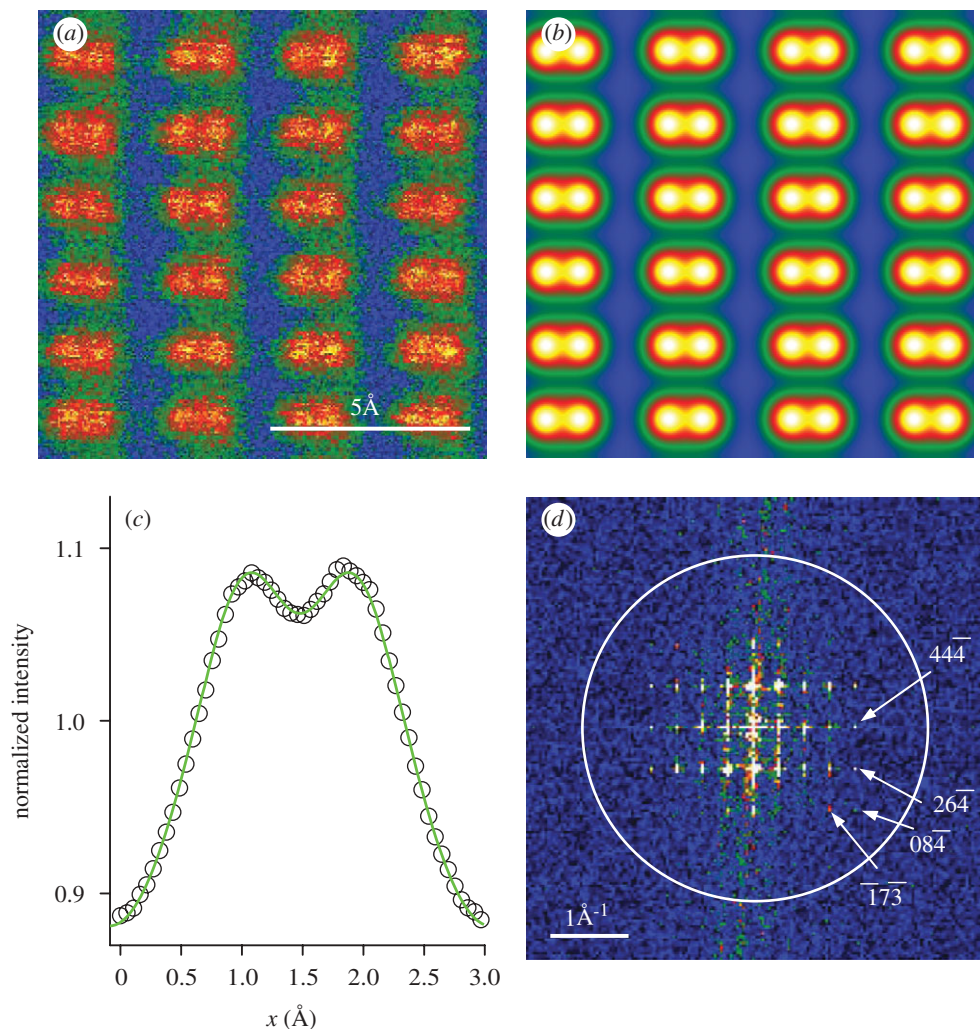
Figure 1. (*a*) Subsection of an experimental ADF image of Si ⟨1 1 2⟩ obtained on the ORNL VG Microscopes HB603U STEM operating at 300 kV with a cold field emission gun, Nion third-order aberration corrector and a detector spanning 90–200 mrad. (*b*) Simulated image for $t = 300\,\text{Å}$, $\Delta f = -45\,\text{Å}$, $C_s = -0.037\,\text{mm}$, $C_5 = 100\,\text{mm}$ and probe-forming aperture of 22 mrad. Temporal and spatial incoherence have been accounted for by convolving with a Gaussian with FWHM of 0.60 Å. (*c*) Line scans averaged over a width of 10 pixels comparing experiment (black circle) and theory (green line). The experimental result has been averaged over a total of 96 dumbbells and normalized by the average of the data points shown. (*d*) Experimental diffractogram with the objective aperture indicated by the white circle showing information transfer to 0.61 Å. Adapted from Peng *et al.* (2008).

Transmission Electron Aberration-corrected Microscope (TEAM) Project of the US Department of Energy (http://ncem.lbl.gov/TEAM-project/). The TEAM 0.5 microscope at Lawrence Berkeley National Laboratory has recently pushed the resolution limit to 0.47 Å, with a confidence level of 60 per cent using Ge ⟨1 1 4⟩ (Erni *et al.* 2009).
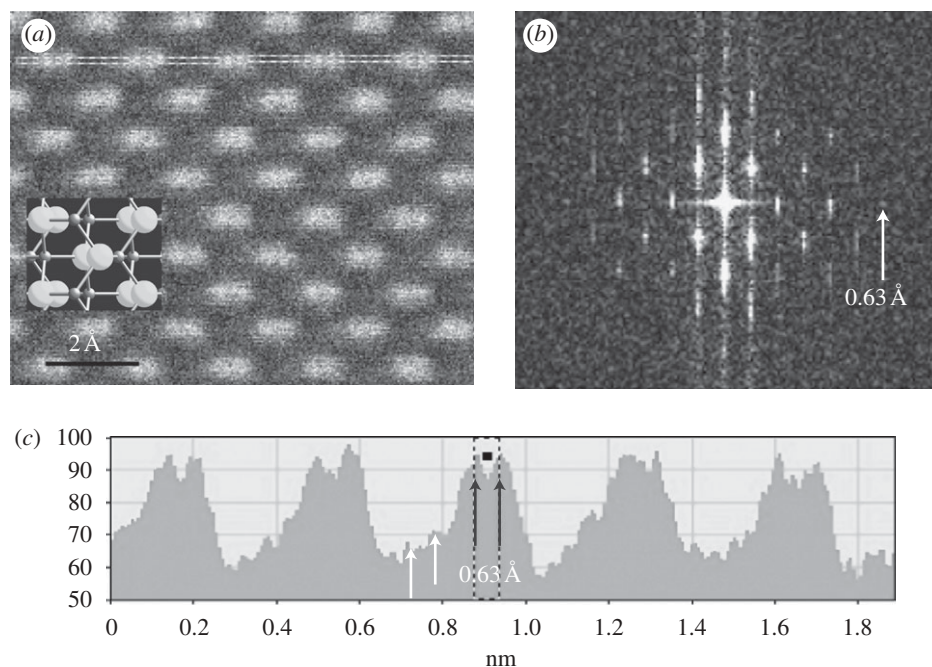
Figure 2. Z-contrast image (*a*) of wurtzite GaN in the ⟨2 1 1⟩ projection, with the structure shown inset, Ga atoms as large spheres, N atoms as small grey spheres, with a line trace from the dashed area (*c*) showing resolution of the Ga dumbbells 0.63 Å apart (black arrows), with the N atoms also just visible (white arrows). The Fourier transform (*b*) shows information transfer to 0.63 Å. Images are raw data from the ORNL FEI Titan 80-300, recorded by A. R. Lupini.

The resolution of spectroscopic images also dramatically improved with aberration correction (for a recent review, see Pennycook *et al.* (2009)), and it is possible to investigate experimentally longstanding issues such as the delocalization of the ionization interaction. Figure 3 shows line profiles obtained from $LaMnO_3$ in the pseudocubic ⟨0 0 1⟩ zone axis along the ⟨1 1 0⟩ direction across La and MnO columns (Oxley *et al.* 2007). La has both a high energy $M_{4,5}$ edge and a low energy $N_{4,5}$ edge, allowing a direct comparison of image contrast. Furthermore, Mn has a high energy $L_{2,3}$ edge, but differs significantly in Z from La; hence, comparing the thickness dependence of the La and Mn columns allows the role of dechannelling to be explored. All experimental traces show reduced contrast compared with simulations, but do not show a simple trend with inner shell binding energy. The La $N_{4,5}$ edge at 99 eV still shows atomic resolution, although the *contrast* is reduced significantly compared with that obtained from the La $M_{4,5}$ edge at around 842 eV. The FWHM of the La $N_{4,5}$ trace is very similar to that of the La $M_{4,5}$ edge, whereas estimates of ionization delocalization show the La $N_{4,5}$ excitation to be much broader (e.g. Howie 1979; Pennycook 1988; Egerton 2007). Such estimates give a good order of magnitude estimate of the mean interaction distance but cannot give an accurate prediction of image contrast for which quantum mechanical simulations are essential (Oxley *et al.* 2007; Oxley & Pennycook 2008). The extended tail of the La $N_{4,5}$ response does not preclude atomic resolution; instead, it reduces the contrast.
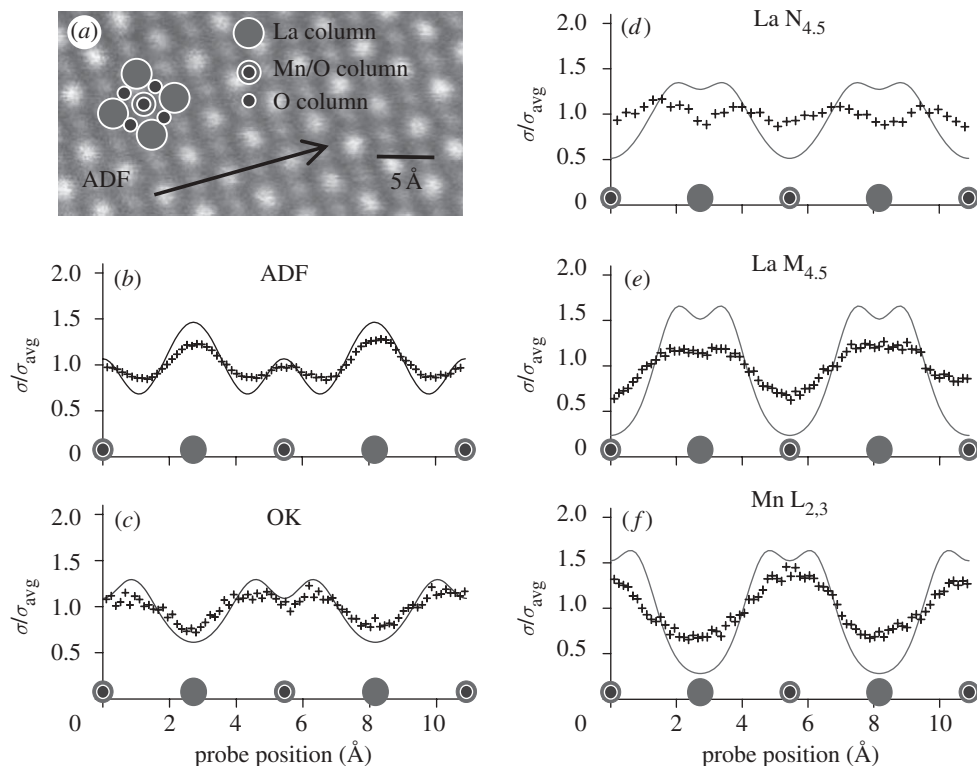
S. J. Pennycook et al.

Figure 3. (*a*) Z-contrast image of $LaMnO_3$ in the pseudocubic $\langle 1\,0\,0 \rangle$ zone axis, with the pseudocubic $\langle 1\,1\,0 \rangle$ direction arrowed, with intensity profiles (normalized to the average intensity) of (*b*) the ADF image and (*c–f*) spectroscopic image profiles for various core losses. Simulations are shown as solid lines and experimental data as crosses, which always show lower contrast. Note the broad volcano-like feature at the O K edge (*c*), despite its high threshold energy (532 eV), which results from the effective non-local nature of the interaction. The Mn $L_{2,3}$ edge (*f*) at slightly higher energy (642 eV) shows much higher contrast, as does the La $L_{2,3}$ edge at 832 eV. Even the La $N_{4,5}$ edge (*d*) at 99 eV shows atomic resolution, although it has a long delocalized tail compared with the other high energy edges that reduce its contrast. Data obtained with a 100 kV aberration-corrected STEM with EELS collection angle 12 mrad. The positions of the atomic columns are indicated by the filled circles. Adapted from Oxley *et al.* (2007).

Many of the simulated images show volcano-like features on the atom sites, dips in intensity when the probe is located over the site. Such features have been confirmed experimentally for the O K and La $N_{4,5}$ edges. Comparing with simulations for very thin crystals shows that the La $N_{4,5}$ volcano is due to dechannelling and scattering of the probe as it propagates along the column (estimated to be 250 Å thick experimentally), whereas in the O case, it is due to the effective non-local nature of the inelastic interaction. Non-local effects are less pronounced as the collection angle into the spectrometer is opened up and the spectroscopic image approaches the ideal incoherent image that is obtained when all elastically scattered electrons are collected (Rose 1976; Ritchie & Howie 1988).
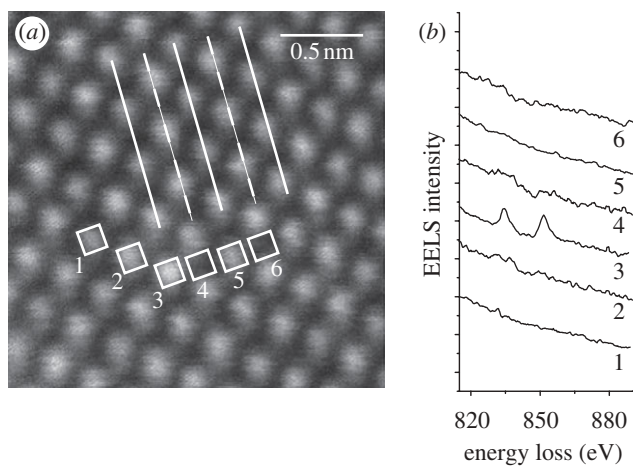
Figure 4. Spectroscopic identification of an individual atom in its bulk environment by EELS. (*a*) Z-contrast image of $CaTiO_3$ showing traces of the CaO and TiO_2 {1 0 0} planes as solid and dashed lines, respectively. A single La dopant atom in column 3 causes this column to be slightly brighter than other Ca columns, and EELS from it shows a clear La $M_{4,5}$ signal. (*b*) Moving the probe to adjacent columns gives reduced or undetectable signals. Adapted from Varela *et al.* (2004).

Besides the decreased FWHM of the aberration-corrected probe, it also has significantly reduced probe tails, meaning that more current is incident on a column of interest and less wasted illuminating surrounding columns, at least in sufficiently thin crystals. This greatly improves the sensitivity of the analysis to the column composition, and figure 4 shows the spectroscopic identification of a single atom inside a bulk material, La in $CaTiO_3$ (Varela *et al.* 2004). In this example, the small residual signal present on the adjacent O column allowed the thickness to be deduced at around 100 Å in comparison with dynamical image simulations.

STEM bright field imaging can be optically equivalent to TEM bright field imaging via the principle of reciprocity or time-reversal symmetry of elastic scattering amplitudes (Cowley 1969; Zeitler & Thomson 1970), when the STEM probe-forming (objective) aperture is equivalent to the TEM objective aperture and the STEM collector aperture is equivalent to the TEM condenser aperture. However, before aberration correction, for phase contrast imaging, a small beam divergence was necessary to avoid averaging over the oscillations of the transfer function and damping the contrast (figure 5*a*). This meant that the STEM collector aperture had to be very much smaller than the objective aperture, and only a small fraction of the incident probe current could be used to form the image. Consequently, STEM phase contrast imaging was very noisy and rarely used. The situation is quite different after aberration correction. Not only is the resolution extended, as seen in figure 5*b*, but now the beam divergence can be much larger without damping the transfer. The STEM collector aperture can be enlarged an order of magnitude, giving around two orders of magnitude increased signal. Of course, still, only a small fraction of the incident probe current is used, meaning that it is less efficient than the equivalent TEM imaging conditions. However, the STEM bright field image is now of
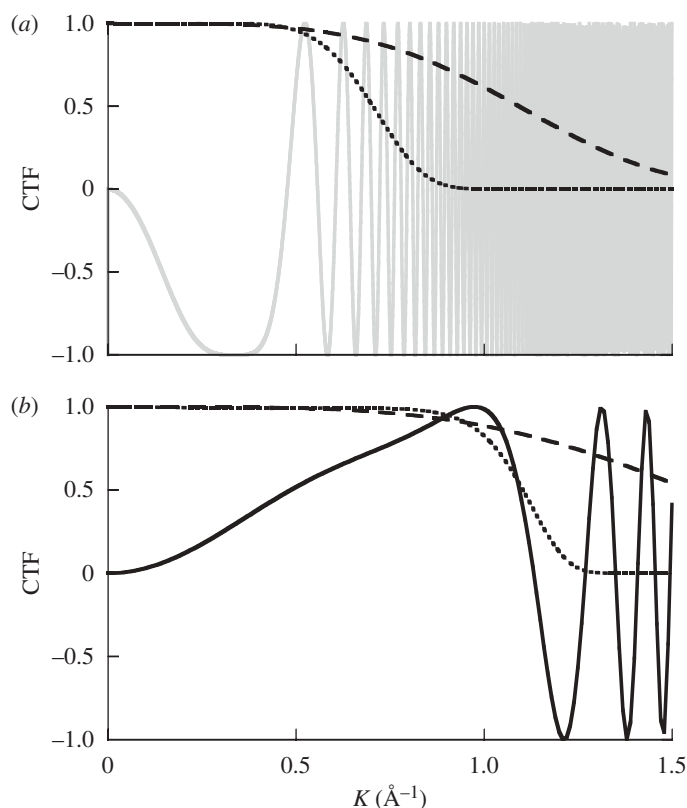
Figure 5. (*a*) Contrast transfer functions for an uncorrected 300 kV microscope, grey line, with a coefficient of third-order spherical aberration $C_s = 1.0$ mm, chromatic aberration $C_c = 1.6$ mm, and defocus $\Delta f = -44$ nm, with the damping envelopes introduced by a beam divergence of 0.25 mrad (dotted line) and an energy spread of 0.6 eV FWHM typical of a Schottky (thermal) field emission source (dashed line). (*b*) Transfer for a corrected 300 kV microscope (solid line) ($C_s = -37$ μm, $C_5 = 100$ mm, $C_c = 1.6$ mm, $\Delta f = 5$ nm), with the damping envelopes introduced by a beam divergence of 2.5 mrad (dotted line) and an energy spread of 0.3 eV typical of a cold field emission source (dashed line). Reproduced from Pennycook *et al.* (2007).

high quality and is available simultaneously with the Z-contrast image with pixel-to-pixel correlation. An example of the simultaneous phase contrast and Z-contrast imaging of $SrTiO_3$ $\langle 1\,1\,0 \rangle$ is shown in figure 6. The O atom columns are just visible in the Z-contrast image in between the Ti columns. If they were spurious features produced by probe tails, then there would be brighter features in between the Sr columns, but, since they are absent, the observed features must indeed be O columns. The optimum defocus and third-order spherical aberration are tuned for the Z-contrast image, but they also result in a good phase contrast image, although the optimum focus is slightly different in the two cases. The phase contrast images show the oxygen columns with stronger contrast (Jia *et al.* 2003; Jia 2004, 2005, 2006).

A less anticipated result of the much reduced depth of focus of the aberration-corrected probe is the ability to perform optical sectioning in a light amorphous or randomly oriented matrix. A through-focal series of images becomes a depth
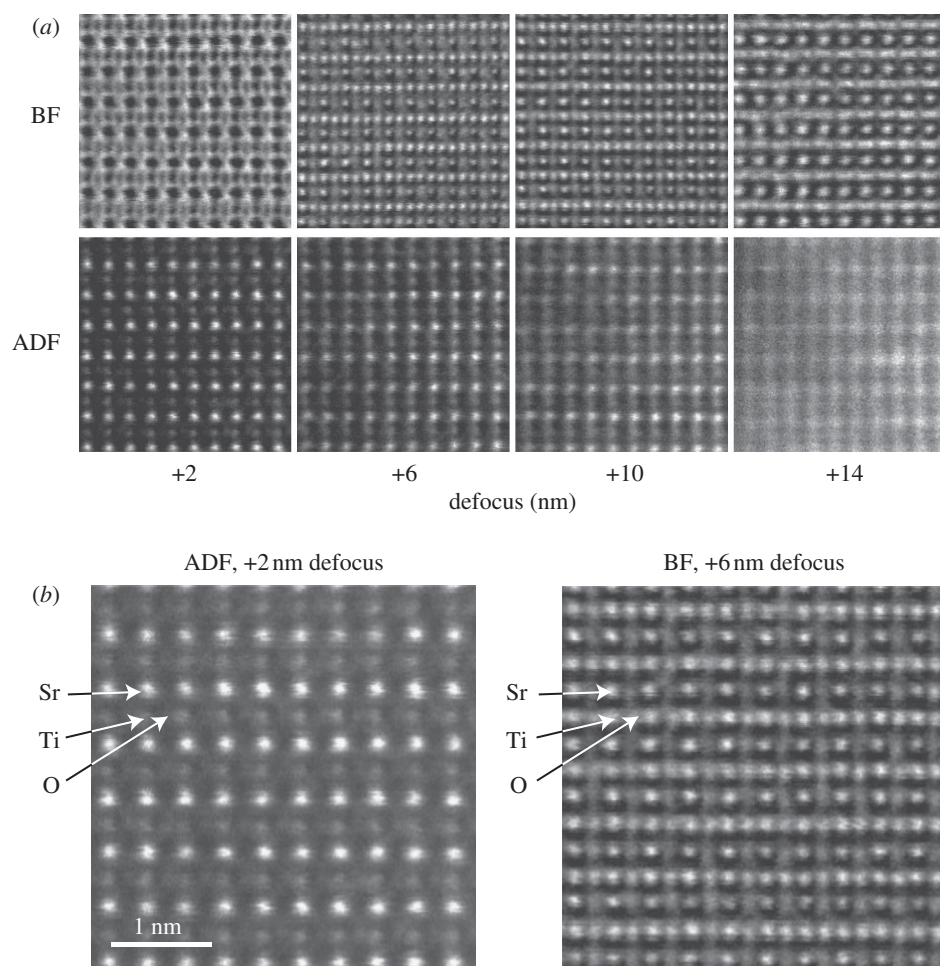
Figure 6. Comparison of coherent and incoherent imaging of $SrTiO_3$ in the $\langle 1\,1\,0 \rangle$ projection using a 300 kV VG Microscopes HB603U STEM with Nion aberration corrector. (*a*) A through-focal series with 4 nm defocus steps, in which the phase contrast images show complex variations in contrast while the incoherent ADF image contrast slowly blurs. All images are raw data and show some instabilities. (*b*) Under optimum conditions, the ADF image shows the Sr columns brightest, the Ti columns less bright and the O columns barely visible, while the phase contrast BF image shows the O columns with high contrast. Microscope parameters are optimized for the smallest probe, with, nominally, a probe-forming aperture of approximately 22 mrad, $C_s \sim -0.037$ mm and $C_5 \sim 100$ mm. Courtesy of M. F. Chisholm, A. R. Lupini and A. Y. Borisevich, adapted from Pennycook (2006).

sequence of images as shown in figure 7 (Borisevich *et al.* 2006*a*). In this example, the atoms are well separated in depth and provide an excellent test of the expected depth resolution of 7–8 nm. The incremental intensity as a function of focus has an FWHM of 12 nm, higher than expected perhaps due to beam broadening or residual aberrations. Because of the high signal-to-noise ratio, the peak intensity can be located to a precision of ± 2 Å with 95 per cent confidence. This is a relatively ideal case, and the presence of a larger background can significantly reduce the range of visibility for single atoms. In a through-focal series of images of
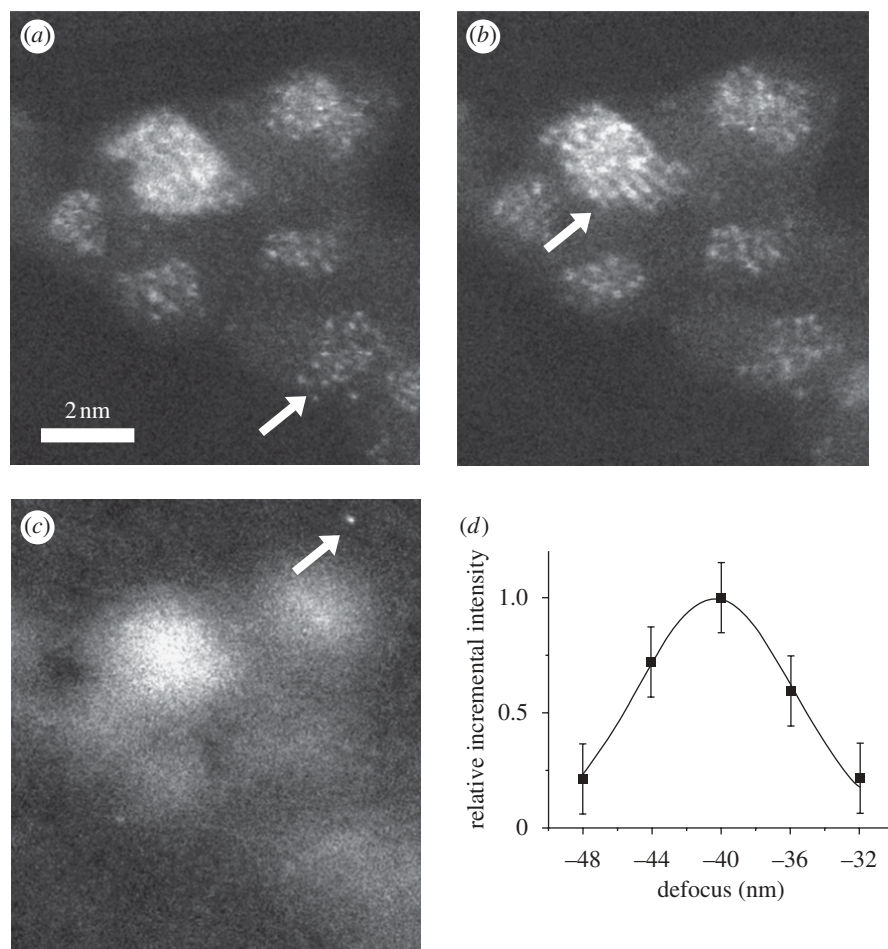
Figure 7. Three frames from a through-focal series of Z-contrast images from a Pt/Ru catalyst on a γ-alumina support, at defocus of (a) -12 nm, (b) -16 nm and (c) -40 nm from the initial defocus setting. Arrows point to regions in focus, and in (c), a single atom is seen in focus on the carbon support film. (d) Integrated intensity of the Pt atom seen in (c) above the level of the carbon film as a function of defocus, compared with a Gaussian fit. The FWHM of the fit is 12 nm, but the precision of the location of the peak intensity is 0.2 nm with 95% confidence. Reproduced from Borisevich *et al.* (2006*a*).

individual Hf atoms in a high dielectric constant semiconductor device structure, the atoms were visible only over a range of approximately 1 nm or so (van Benthem *et al.* 2005, 2006).

The situation is more complicated in a crystal aligned to a zone axis. Optical sectioning is now opposed by the tendency of the columns to channel the electrons. Beams incident near the optic axis couple efficiently into the 1 s Bloch state, which before aberration correction was the dominant contribution to the ADF image (Pennycook & Jesson 1990, 1991; Jesson & Pennycook 1993, 1995; Nellist & Pennycook 1999). After aberration correction, the outer beams passing through the outer regions of the objective aperture are now so far from the
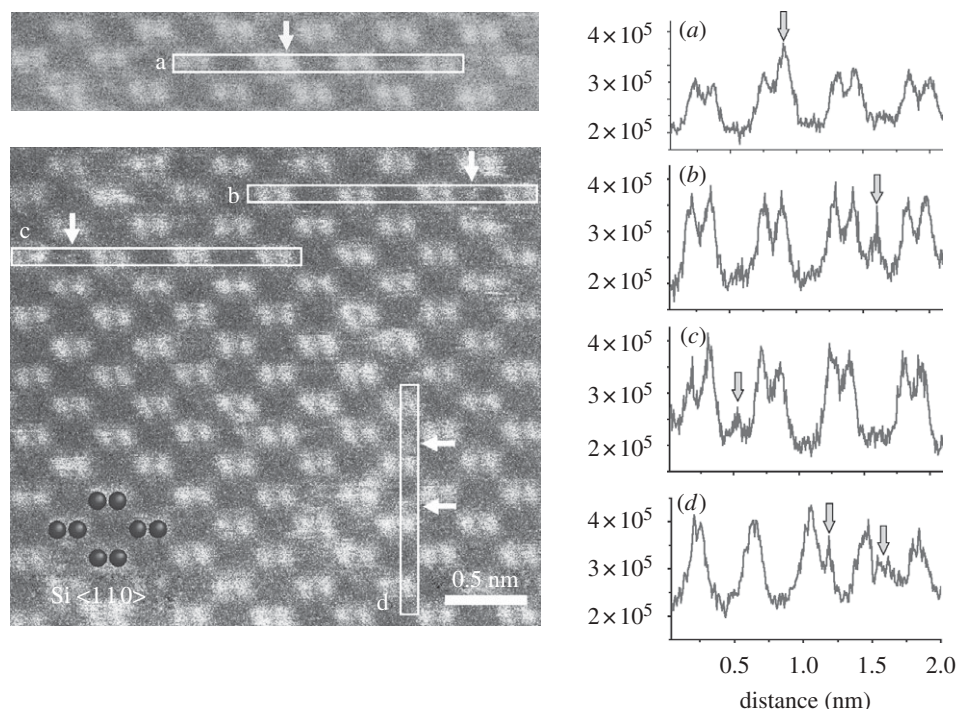
Figure 8. HAADF images of a Si nanowire in $\langle 1\,1\,0 \rangle$ zone-axis orientation (left panel). A slight image distortion caused during the scan was unwarped. Boxes show the regions used for intensity profiles, with Au atoms in various configurations arrowed; (*a*) substitutional; (*b*) tetrahedral; (*c*) hexagonal; (*d*) buckled Si–Au–Si chain configurations. The intensity profiles across the Si dumbbells correspond to a width of 18 pixels. Adapted from Oh *et al.* (2008).

zone axis that they do not channel strongly and therefore still tend to come to a focus as if propagating in free space. This effect was first seen in a Bloch wave analysis of ADF STEM imaging with large probe-forming apertures (Peng *et al.* 2004). The competition of the two probe components depends on the channelling strength of the column. Calculations for Si $\langle 1\,1\,0 \rangle$-containing Bi atoms at various depths predicted that individual Bi atoms at different depths could be selectively brought into focus (Borisevich *et al.* 2006*b*; see also Cosgriff & Nellist 2007). However, this was not the case for La atoms in $CaTiO_3$. Similar depth-dependent effects are predicted for electron energy loss spectroscopy (EELS), where the ability to elementally select a particular species is an advantage (D'Alfonso *et al.* 2007). A disadvantage of the optical sectioning approach is that the depth resolution for extended objects is much worse, given by d/α, where d is the object diameter and α is the objective aperture semiangle. This is overcome with a true confocal mode in a double-corrected instrument (Nellist *et al.* 2006, 2008).

Figure 8 shows the images of individual Au atoms inside a Si nanowire in the $\langle 1\,1\,0 \rangle$ orientation obtained by optical sectioning. The beam is brought to a focus inside the thickness of the wire so that surface atoms are no longer in focus (Oh *et al.* 2008). Hence, the Au atoms visible in the image are definitely located
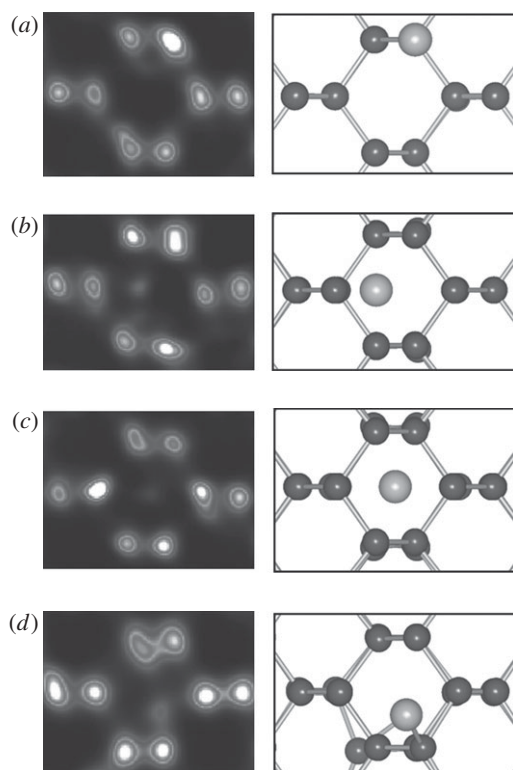
Figure 9. Local views of defect configurations of Au in Si. (*a*) Substitutional; (*b*) tetrahedral; (*c*) hexagonal; (*d*) buckled Si–Au–Si chain configurations. The HAADF images (left panels) were processed by maximum entropy image deconvolution (HREM Inc.) using a Lorentzian-type probe function. The corresponding atomic models (right panels) calculated by density functional theory match the images closely. Adapted from Oh *et al.* (2008).

inside the bulk of the wire, although they may well be injected there by knock-on processes since they are observed to be quite mobile, moving between successive images. Nevertheless, a substitutional and three interstitial configurations—a tetrahedral, a hexagonal and a buckled Si–Au–Si chain configuration—are seen. Density functional calculations confirm that these are stable sites for Au atoms (figure 9), and calculated formation energies are in accord with the number densities observed in the images. However, the number densities imply an effective temperature of around 1000 °C, another indication that they are metastable configurations induced by the electron beam.

Optical sectioning combined with density functional theory has also been applied to high dielectric constant semiconductor device structures. The three-dimensional distribution of stray Hf atoms was determined by optical sectioning (van Benthem *et al.* 2005, 2006). A relatively high density was seen in the 1 nm thick SiO_2 layer, but, in this case, the Hf atoms were not affected by the 300 kV beam. No Hf atoms were found at the critical Si/SiO_2 interface, a result explained by density functional calculations that showed interfacial Hf atoms to have 1.4 eV energy higher than those away from the interface (Marinopoulos *et al.* 2008).
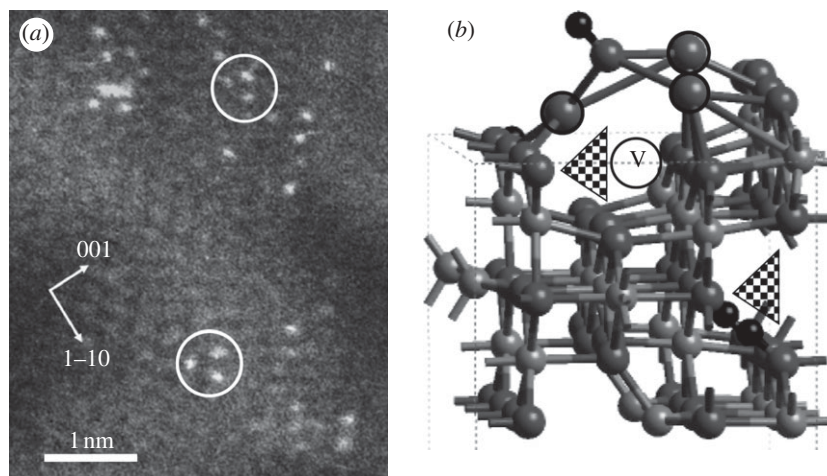
Figure 10. (*a*) Z-contrast STEM image of Pt on the surface of γ-Al$_2$O$_3$ close to the $\langle 1\,1\,0 \rangle$ orientation. Two Pt$_3$ trimer structures are circled. (*b*) Schematic of the configuration for the Pt$_3$OH unit on the {1 1 0} surface of γ-Al$_2$O$_3$, determined by first-principles calculations; Pt atoms shown circled. The circled V marks a vacant tetrahedral cation site; triangles mark possible H atom positions in the vacancy. Adapted from Sohlberg *et al.* (2004).

Calculations further showed that significant leakage currents could occur across the device at the observed Hf densities, as was indeed found experimentally in this particular sample.

3. Application to catalysts

Catalysts often comprise heavy transition metals on a light support, which is an ideal situation for ADF STEM imaging. While single atoms could be detected prior to aberration correction (Nellist & Pennycook 1996), after correction the image quality is significantly enhanced, allowing accurate extraction of Pt atom positions as shown in figure 10 (Sohlberg *et al.* 2004). In the case of the Pt$_3$ trimers, two of the spacings were found to be too large for a metallic bond, and the image could only be matched to density functional calculations by assuming the trimer to be capped by an OH group. The combination of density functional theory and imaging has proved quite illuminating concerning the nature and catalytic activity of several transition metal systems. In the case of the Rh/γ-alumina catalytic system, the raft-like structures observed with the microscope were identified by comparison with simulations of the high-pressure phase of Rh sesquioxide. The denser structure of the high-pressure Rh$_2$O$_3$ phase gives a better 'lattice match' to the Al$_2$O$_3$ structure (Sohlberg *et al.* 2008).

γ-Alumina is a common catalytic support, which is often stabilized thermally by the addition of La. However, controversy existed over the mechanism involved. Images of single La atoms on the γ-alumina support showed them to be widely separated and located over Al–O positions on the {1 0 0} surface, as opposed to the {1 1 0} surface that is stable in the undoped alumina. Calculations showed that the origin of stabilization was a much higher binding energy on

γ-alumina (7.5–9 eV) than on the α-alumina (4–5 eV), which is the product of the undesirable high-temperature phase transformation. The La atoms increase the energy cost of the phase transformation, increasing the transition temperature (Wang *et al.* 2004). In the case of chromia/alumina catalytic systems, it was found that the rate of degradation with a γ-alumina support was very rapid, but replacing the support with η-alumina greatly improves stability. The effect is quite remarkable because the two structures differ only in the distribution of the structural vacancies. In γ-Al$_2$O$_3$, most of the vacancies are located in tetrahedral sites, whereas, in η-Al$_2$O$_3$, they are distributed mainly in the octahedral sites (Zhou & Snyder 1991). However, the difference significantly affects the surface relaxation processes in these polytypes that result in their different surface reactivity (Sohlberg *et al.* 1999). The difference means that Cr clusters on the γ-alumina surface but remains highly dispersed on the η-alumina surface, and hence catalytically active (Borisevich *et al.* 2007).

Finally, we show how aberration-corrected STEM and first-principles theory elucidated the mechanism for the low-temperature oxidation of CO to CO$_2$ by Au nanoparticles (Rashkeev *et al.* 2007). Au is inactive in the bulk form, but nanoscale Au catalyses the reaction even below room temperature, and many explanations have been proposed (Bamwenda *et al.* 1997; Valden *et al.* 1998; Yoon *et al.* 2003). Figure 11 shows images of the catalyst prepared by deposition/precipitation onto nanocrystalline anatase (Zhu *et al.* 2004). In the as-deposited state, many individual Au atoms can be seen, but after reduction to the active form, the atoms are much less visible. The melting point of Au nanoparticles reduces with diameter and reaches room temperature at approximately the size range observed (Buffat & Borel 1976). Therefore, it seems likely that the smallest nanoparticles may be in a quasi-liquid state. Most of the reduced nanoparticles are 1–2 nm in diameter, and quantifying the thicknesses by comparing with image simulations revealed that a high fraction is just one or two monolayers thick.

First-principles calculations were carried out on a whole sequence of nanoparticles with different sizes and atomic configurations on anatase. The key feature for the activity of the nanoparticles relative to bulk Au is the presence of low-coordination sites. As shown in figure 12, with reducing coordination number, the energy required to desorb O$_2$ exceeds the activation barrier for the reaction for a coordination number less than 5. This means that an O$_2$ molecule can reside on the surface long enough to react with an adsorbed CO molecule. At sites with coordination number 6 or greater, desorption will occur on average before the reaction proceeds, and the surface of the Au nanoparticle will become inactive for the reaction. In this situation, only perimeter sites can still participate significantly in the reaction. This is the underlying reason for the vast change in catalytic behaviour for nanoscale Au (see Rashkeev *et al.* (2007) for details and further references). The low activation barrier on the Au nanoparticle is partly due to the 'looseness' of the Au–Au bonds, as proposed by Yoon *et al.* (2003), which allows the molecules to move during the reaction and find a configuration that minimizes the activation barrier, as shown in figure 12*b*. First-principles Car–Parrinello molecular dynamics calculations of a Au$_{10}$ cluster on anatase at a temperature of 200 K indicated atomic displacements in the region of 0.6–0.7 Å, sufficiently high to preclude any atomic resolution imaging.
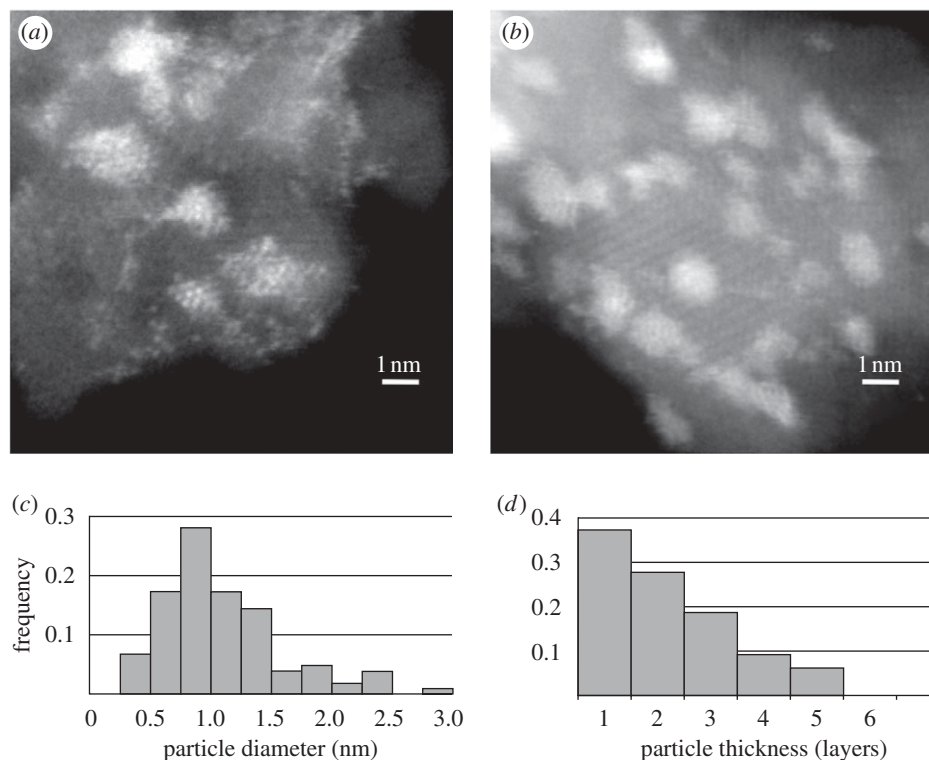
Figure 11. Z-contrast images of Au nanoparticles deposited on nanocrystalline anatase by deposition/precipitation, (*a*) as deposited, with Au atoms resolved, and (*b*) after reduction to the active form. The average particle size is around 1 nm (*c*) and many particles are only one monolayer in thickness (*d*). Reproduced from Rashkeev *et al.* (2007).

4. Semiconductor quantum wires

Controlled growth of semiconductor quantum nano-object arrays is important for reproducible fabrication of optoelectronic devices to achieve high efficiency. The sublattice sensitivity of aberration-corrected Z-contrast imaging, combined with elasticity calculations, has revealed the nucleation sites for nanowires and allowed quantitative understanding of the growth of stacked, strained layer nanowire arrays. Figure 13 shows a cross-sectional view of an $InAs_xP_{1-x}$ nanowire array sandwiched between InP layers, grown by molecular beam epitaxy (Fuster *et al.* 2004). It is clear that the array is not vertical but canted to the right. The origin of this effect can be traced to the nucleation process. Atomic force microscopy examination of the nanowires deposited on an InP substrate showed the tendency for the nanowires to be located near step edges. While many of the steps were wavy, some wires nucleated near straight segments of steps, and these gave a clear sharp image in cross-section Z-contrast images, as shown in figure 14 (Molina *et al.* 2007). In this $\langle 1\,1\,0 \rangle$ projection, the cubic zinc-blende structure projects as dumbbells with the In column towards the left of the figure and the P or As_xP_{1-x} column towards the right. The image has its threshold
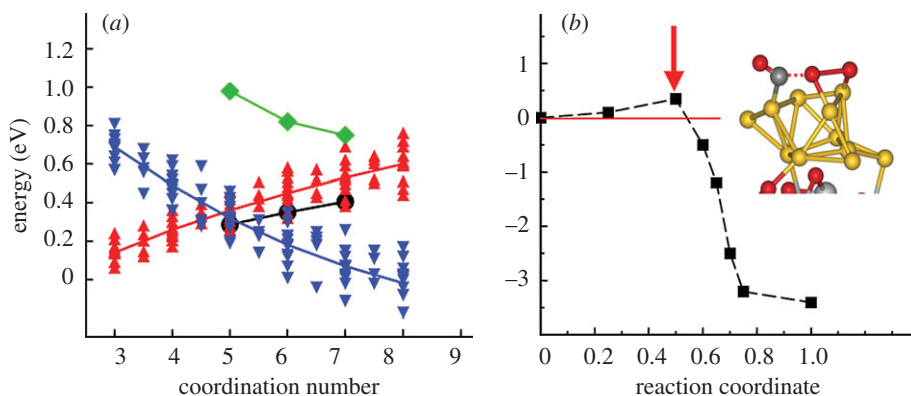
Figure 12. (*a*) Calculated desorption energies (E_d) for (O_2) molecules bound to Au nanoparticle sites as a function of coordination number, and the activation barrier (E_r) for conversion of CO to CO_2 (blue line, E_d; green line, $E_{d,p}$; red line; E_r; black line, $E_{r,p}$). The desorption energy exceeds the reaction barrier below a coordination number of 5, which allows the reaction to proceed on the nanoparticle surface. Above this coordination number, only perimeter sites are important. (*b*) An example of the activation barrier for the CO to CO_2 reaction, in which the flexibility of the Au nanocluster lowers the activation barrier at the transition state marked by the red arrow, a feature critical to achieving high activity at room temperature. The schematic shows the nanocluster in its transition state, with Ti in grey, O in red and Au in gold. Reproduced from Rashkeev *et al.* (2007).
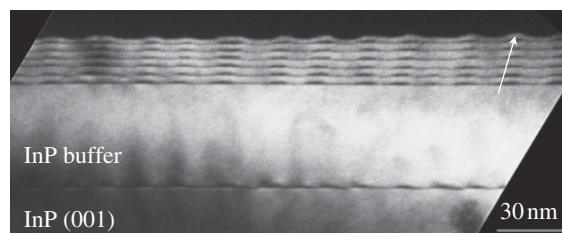

Figure 13. Low magnification TEM diffraction contrast image of an $InAs_xP_{1-x}$ nanowire array sandwiched between InP layers, showing that the alignment of the nanowire stack is offset from the growth direction. Adapted from Fuster *et al.* (2004).

at the intensity level corresponding to the P column, so that the interface between the InP layer and the nanowire can be located to atomic precision. It is seen that the transition from the substrate InP layer to the nanowire is atomically abrupt. The location of the step is slightly offset from the centre of the nanowire, indicating that the initial nucleation took place on the upper terrace of the step.

Nucleation on the upper terrace is entirely in accord with expectations based on the 3.2 per cent lattice mismatch between InAs and InP. Because of the existence of the step, a few unit cells next to the step on the upper terrace can relax sideways a little, reducing the lattice mismatch, and therefore making this area the preferential nucleation site. Finite-element elasticity calculations showed that
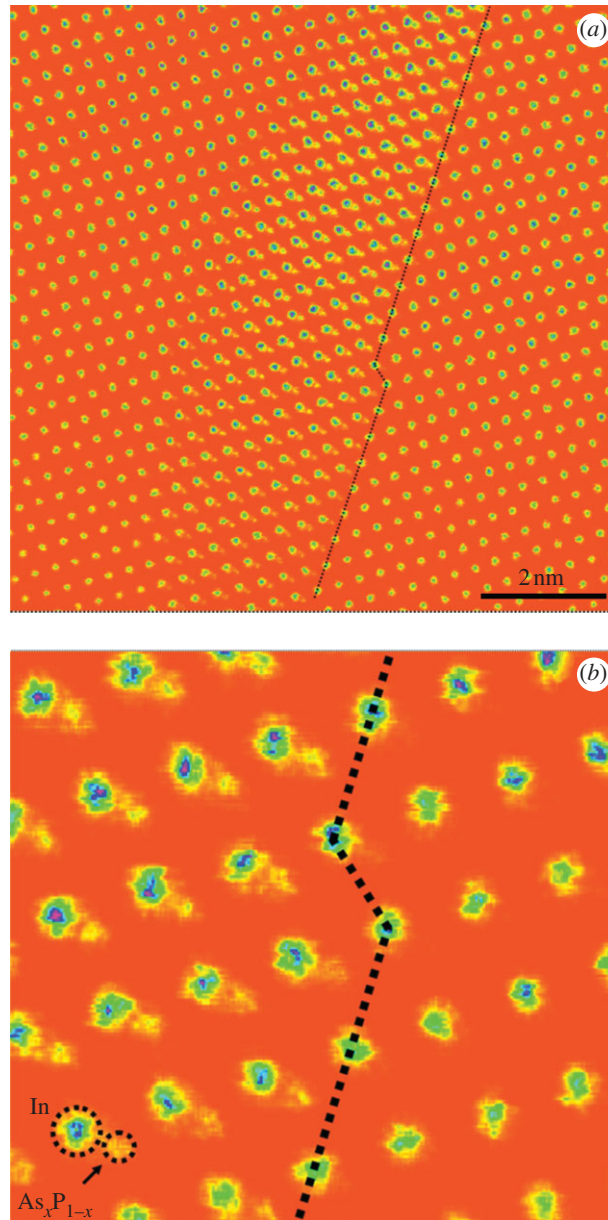
Figure 14. (a) Z-contrast image of the $InAs_xP_{1-x}$ nanowire. The image has been coloured and has its threshold at the intensity level of the P columns to highlight the As_xP_{1-x} columns in the nanowires. (b) Higher magnification view showing the atomically abrupt transition from the InP to the $InAs_xP_{1-x}$ nanowire, with an interface step present under the nanowire. Reproduced from Molina *et al.* (2007).

the magnitude of the relaxation was indeed significant. With the nucleation taking place on the upper terrace, the surface of the growing film will roughen, so this represents the onset of the Stranski–Krastanov transition from a two-dimensional to a three-dimensional growth mode.

It can also be seen in figure 14*a* that there is a slight asymmetry in the As distribution within the wire, the region above the upper terrace showing brighter and therefore containing more As. This is typical and was also confirmed by quantitative EELS, using the P edge intensity in the barrier layers as calibration. The resulting As concentration maps were used as input into a finite-element elasticity calculation (Molina *et al.* 2006). Owing to the microscopic asymmetry of the As distribution, an anisotropy appeared in the stress on the surface of the subsequent InP barrier layer, with the peak stress emanating from the nanowire appearing slightly offset from the geometric centre of the wire. Therefore, the favourable nucleation site for the next nanowire is slightly offset from the centre of the underlying wire. With carefully controlled conditions, all nanowires line up at a specific angle to the growth direction and the observed angle is in quantitative agreement with the finite-element calculations.

5. Colossal ionic conductivity in Y_2O_3-stabilized ZrO_2/SrTiO$_3$ superlattices

Solid oxide fuel cells (SOFCs) are a promising non-polluting technology for the substitution of fossil fuels, but the conversion efficiency of chemical into electrical energy is limited by the transport of oxygen anions through an electrolyte (Steele & Heinzel 2001). Yttria-stabilized zirconia $(Y_2O_3)_x(ZrO_2)_{1-x}$ (YSZ) is the material most commonly used in SOFCs owing to its mechanical stability, chemical compatibility with electrodes and its high oxygen ionic conductivity. A maximum value of $0.1\,S\,cm^{-1}$ at $1000°C$ is observed for 8–9 mol% yttria content. However, a severe limitation of this material is its relatively low room temperature ionic conductivity, which imposes high operational temperatures, around $800°C$. There is a major research effort devoted to the search for new materials with greatly enhanced ionic conductivity (often referred to as superionic conductors), but it has not yet been successful in reaching the conductivity value desired for applications, at least $0.01\,S\,cm^{-1}$, with operation close to room temperature.

Superlattices comprising strained layers of YSZ between SrTiO$_3$ (STO) spacers have recently been found to show up to eight orders of magnitude enhanced O ion conductivity near room temperature (Garcia-Barriocanal *et al.* 2008), creating intense interest for their potential to achieve high efficiency SOFCs at low operating temperatures. The conductivity was found to scale with the number of interfaces, but was independent of the thickness of the YSZ layer, except when the layer thickness exceeded six to eight unit cells when relaxation set in and the effect disappeared. The contribution of electronic conductivity through the STO was found to be three to four orders of magnitude lower, demonstrating the ionic nature of the conductivity. Furthermore, experiments also ruled out a protonic contribution to the conductance, proving the mobile species to be oxygen ions (see electronic supplementary material in Garcia-Barriocanal *et al.* 2008). Both X-ray and STEM analysis of the strained thin layers showed them to be highly coherent with the YSZ lattice rotated 45° to that of the STO. Figure 15*a* shows a low magnification Z-contrast image of a nine-layer superlattice of 1 nm (two unit cells) thick YSZ layers between STO barriers and a high magnification view showing the cation lattice to be continuous across the YSZ layer.

Insight into the nature of the interface is provided by EELS. Figure 15*b* compares spectra from the interface plane with spectra from the centre of the STO layer. No detectable change is seen in the Ti fine structure, indicating that a Ti 4+ configuration is predominant at the interface plane, which is consistent with the lack of electronic conductivity. However, changes are seen in the O fine structure, indicating a change in coordination, which would be expected since the O sublattices of YSZ and STO are different and incompatible across the interface. Determination of the STO-terminating plane at the interface is provided by the spectrum image shown in figure 16*a*. Comparing the Sr M_3 and Ti $L_{2,3}$ profiles across the interface shows that on both sides the Sr edge drops before the Ti edge, so that the STO is terminated at the TiO_2 plane. Now from the cation positions visible in the image (figure 15), it is apparent that the structure is as shown in figure 16*b*. While the distance between the TiO_2 plane and the Zr plane is sufficient for O ions to be present, the perovskite and fluorite structures demand different O positions. This may give rise to an enhanced number of oxygen vacancies (shown shaded in the model) and structural disorder necessary to explain the origin of the colossal ionic conductivity. Perhaps this plane could be better thought of as more like a vacancy liquid than a solid oxide, exhibiting liquid-like diffusivities.

6. Future possibilities for aberration-corrected scanning transmission electron microscopy

Aberration correction allows the pole piece gap to be opened up without a major cost in resolution, so that there is more space for special holders for heating or cooling or for *in situ* observations. Particularly appealing is the possibility of using thin SiN windows for imaging in high-pressure or corrosive environments. With a 300 kV aberration-corrected incident beam, a 20 nm thick window would give minimal broadening of the probe and should still allow atomic resolution to be achieved for objects near the entrance window.

Many more possibilities exist for mapping functionality in energy conversion devices such as solar cells or materials for solid-state lighting. A cathodoluminescence detector in an aberration-corrected STEM would allow light emission to be correlated to dislocation core structure and impurity content (Pennycook 2008) and perhaps enable the actual non-radiative pathways to be determined and eliminated. Similarly, EBIC could provide maps of charge collection efficiency in solar cells. Operating devices have already been observed in STEM at low resolution using cathodoluminescence (Bunker *et al.* 2005) and EBIC (Progl *et al.* 2008). Extending these studies to the aberration-corrected STEM, in conjunction with theory, could provide key insights into the carrier dynamics in the vicinity of defects and how they change as a function of operating current. Addition of a scanning tunnelling microscope to the STEM would allow bias to be applied to local regions of sample, inducing local fields and band bending and the effect on local electronic and optical properties to be investigated.

It is apparent that the era of aberration-corrected microscopy will provide new means to connect structure to functionality. *In operandi* imaging of catalysts will become feasible, although care should be taken to avoid beam-induced effects,
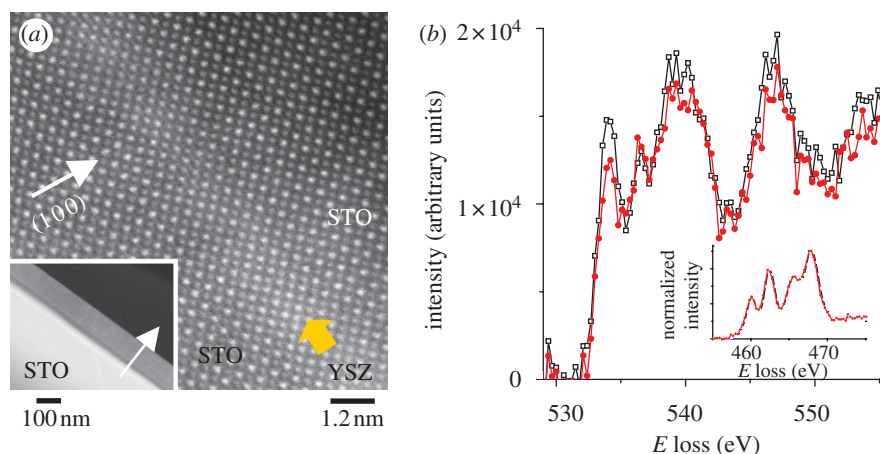
Figure 15. (*a*) Z-contrast STEM image of the STO/YSZ interface of the $(YSZ_{1\,nm}/STO_{10\,nm})_9$ superlattice (with nine repeats), obtained in the VG Microscopes HB603U microscope. A yellow arrow marks the position of the YSZ layer. The inset is a low magnification image obtained in the VG Microscopes HB501UX. In both cases, a white arrow shows the growth direction. (*b*) EEL spectra showing the O K edge obtained from the STO unit cell at the interface plane (red circles) and 4.5 nm into the STO layer (black squares). The inset shows the Ti $L_{2,3}$ edges for the same positions, same colour code. Reproduced from Garcia-Barriocanal *et al.* (2008).

and the ability to study energy conversion processes in materials and devices will be greatly enhanced. Electron microscopy, in conjunction with theory, could therefore play a critical role in solving the pressing energy problems facing us today.
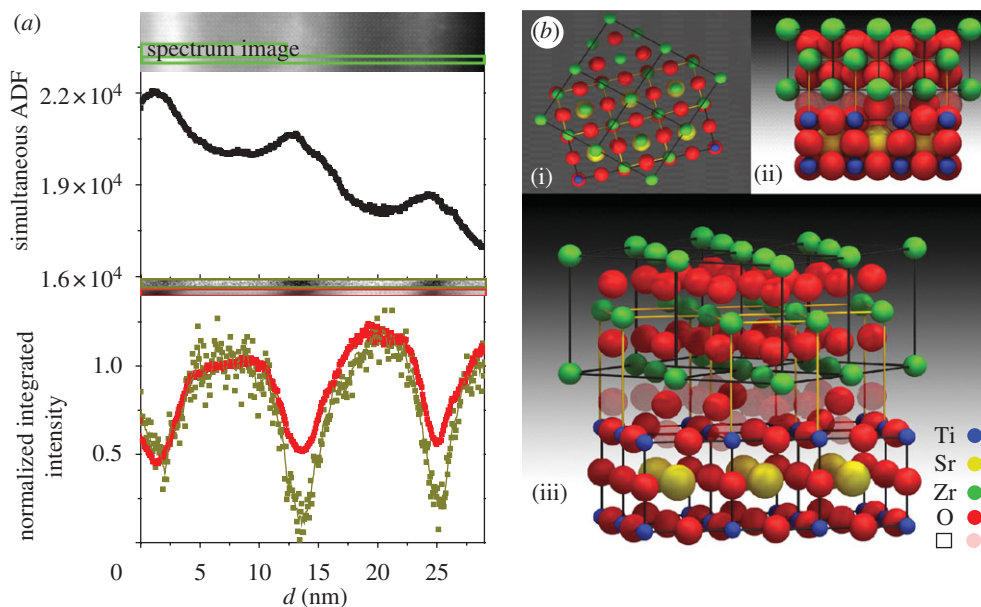
Figure 16. (*a*) EELS chemical maps. The ADF image in the upper panel shows the area used for EELS mapping (spectrum image, marked with a green rectangle) in the $(YSZ_{1\,nm}/STO_{10\,nm})_9$ superlattice. The middle panel shows the averaged ADF signal acquired simultaneously with the EEL spectrum image, showing the STO (low-intensity regions) and YSZ (higher intensity) layers. The lower panel shows the Ti (red) and Sr (dark yellow) EELS line traces across several consecutive interfaces. These line traces are averaged from the elemental two-dimensional images shown in the insets, each framed with the same colour code (red for Ti, dark yellow for Sr). Data obtained in the VG Microscopes HB501UX. As the STEM specimen was relatively thick, several tens of nanometres, the wide chemical interface profiles are most likely due to beam broadening. (*b*) Solid spheres model of the YSZ/STO interface showing: (i) the compatibility of the perovskite and fluorite (rotated) structures; (ii) a side view of the interface between STO (at the bottom) and YSZ (on top) with realistic ionic radius; the shaded oxygen positions in the interface plane are presumed absent or displaced owing to volume constraints, enabling the high ionic conductivity; and (iii) a three-dimensional view of the interface, with the ionic radius reduced by half to better visualize the plane of oxygen vacancies introduced in the interface. Note that the square symbol in the legend represents the empty positions available for oxygen ions at the interface. Reproduced from Garcia-Barriocanal *et al.* (2008).

References

Bamwenda, G. R., Tsubota, S., Nakamura, T. & Haruta, M. 1997 The influence of the preparation methods on the catalytic activity of platinum and gold supported on TiO_2 for CO oxidation. *Catal. Lett.* **44**, 83–87. (doi:10.1023/A:1018925008633)

Batson, P. E., Dellby, N. & Krivanek, O. L. 2002 Sub-angstrom resolution using aberration corrected electron optics. *Nature* **418**, 617–620. (doi:10.1038/nature00972)

Borisevich, A. Y., Lupini, A. R. & Pennycook, S. J. 2006*a* Depth sectioning with the aberration-corrected scanning transmission electron microscope. *Proc. Natl Acad. Sci. USA* **103**, 3044–3048. (doi:10.1073/pnas.0507105103)

Borisevich, A. Y., Lupini, A. R., Travaglini, S. & Pennycook, S. J. 2006*b* Depth sectioning of aligned crystals with the aberration-corrected scanning transmission electron microscope. *J. Electron Microsc.* **55**, 7–12. (doi:10.1093/jmicro/dfi075)

Borisevich, A. Y., Wang, S. W., Rashkeev, S. N., Glazoff, M., Pennycook, S. J. & Pantelides, S. T. 2007 Dual nanoparticle/substrate control of catalytic dehydrogenation. *Adv. Mater.* **19**, 2129–2133. (doi:10.1002/adma.200601618)

Bosman, M., Keast, V. J., Garcia-Munoz, J. L., D'Alfonso, A. J., Findlay, S. D. & Allen, L. J. 2007 Two-dimensional mapping of chemical information at atomic resolution. *Phys. Rev. Lett.* **99**, 086102. (doi:10.1103/PhysRevLett.99.086102)

Buffat, P. & Borel, J.-P. 1976 Size effect on the melting temperature of gold particles. *Phys. Rev. A* **13**, 2287–2298. (doi:10.1103/PhysRevA.13.2287)

Bunker, K. L., Garcia, R. & Russell, P. E. 2005 Scanning electron microscopy cathodoluminescence studies of piezoelectric fields in an InGaN/GaN quantum-well light-emitting diode. *Appl. Phys. Lett.* **86**, 082108. (doi:10.1063/1.1868886)

Chisholm, M. F. & Pennycook, S. J. 2006 Direct imaging of dislocation core structures by Z-contrast STEM. *Phil. Mag.* **86**, 4699–4725. (doi:10.1080/14786430600778757)

Cosgriff, E. C. & Nellist, P. D. 2007 A Bloch wave analysis of optical sectioning in aberration-corrected STEM. *Ultramicroscopy* **107**, 626–634. (doi:10.1016/j.ultramic.2006.12.004)

Cowley, J. M. 1969 Image contrast in a transmission scanning electron microscope. *Appl. Phys. Lett.* **15**, 58–59. (doi:10.1063/1.1652901)

D'Alfonso, A. J., Findlay, S. D., Oxley, M. P., Pennycook, S. J., van Benthem, K. & Allen, L. J. 2007 Depth sectioning in scanning transmission electron microscopy based on core-loss spectroscopy. *Ultramicroscopy* **108**, 17–28. (doi:10.1016/j.ultramic.2007.02.026)

Egerton, R. F. 2007 Limits to the spatial, energy and momentum resolution of electron energy-loss spectroscopy. *Ultramicroscopy* **107**, 575–586. (doi:10.1016/j.ultramic.2006.11.005)

Erni, R., Rossell, M. D., Kisielowski, C. & Dahmen, U. 2009 Atomic resolution imaging with a sub-50 pm electron probe. *Phys. Rev. Lett.* **102**, 096101. (doi:10.1103/PhysRevLett.102.096101)

Fuster, D., Gonzalez, M. U., Gonzalez, L., Gonzalez, Y., Ben, T., Ponce, A. & Molina, S. I. 2004 Stacking of InAs/InP(001) quantum wires studied by *in situ* stress measurements: role of inhomogeneous stress fields. *Appl. Phys. Lett.* **84**, 4723–4725. (doi:10.1063/1.1759374)

Garcia-Barriocanal, J., Rivera-Calzada, A., Varela, M., Sefrioui, Z., Iborra, E., Leon, C., Pennycook, S. J. & Santamaria, J. 2008 Colossal ionic conductivity at interfaces of epitaxial $ZrO_2 : Y_2O_3/SrTiO_3$ heterostructures. *Science* **321**, 676–680. (doi:10.1126/science.1156393)

Haider, M., Uhlemann, S., Schwan, E., Rose, H., Kabius, B. & Urban, K. 1998 Electron microscopy image enhanced. *Nature* **392**, 768–769. (doi:10.1038/33823)

Howie, A. 1979 Image-contrast and localized signal selection techniques. *J. Microsc. Oxford* **117**, 11–23.

Jesson, D. E. & Pennycook, S. J. 1993 Incoherent imaging of thin specimens using coherently scattered electrons. *Proc. R. Soc. Lond. A* **441**, 261–281. (doi:10.1098/rspa.1993.0060)

Jesson, D. E. & Pennycook, S. J. 1995 Incoherent imaging of crystals using thermally scattered electrons. *Proc. R. Soc. Lond. A* **449**, 273–293. (doi:10.1098/rspa.1995.0044)

Jia, C. L. 2004 Atomic-resolution measurement of oxygen concentration in oxide materials. *Science* **303**, 2001–2004. (doi:10.1126/science.1093617)

Jia, C. L. 2005 Atomic-scale analysis of the oxygen configuration at a $SrTiO_3$ dislocation core. *Phys. Rev. Lett.* **95**, 225506. (doi:10.1103/PhysRevLett.95.225506)

Jia, C. L. 2006 Atom vacancies at a screw dislocation core in $SrTiO_3$. *Phil. Mag. Lett.* **86**, 683–690. (doi:10.1080/09500830600965087)

Jia, C. L., Lentzen, M. & Urban, K. 2003 Atomic-resolution imaging of oxygen in perovskite ceramics. *Science* **299**, 870–873. (doi:10.1126/science.1079121)

Kisielowski, C. *et al.* 2008 Detection of single atoms and buried defects in three dimensions by aberration-corrected electron microscope with 0.5-angstrom information limit. *Microsc. Microanal.* **14**, 469–477. (doi:10.1017/s1431927608080902)

LeBeau, J. M., Findlay, S. D., Allen, L. J. & Stemmer, S. 2008 Quantitative atomic resolution scanning transmission electron microscopy. *Phys. Rev. Lett.* **100**, 206101. (doi:10.1103/PhysRevLett.100.206101)

Lupini, A. R. & Pennycook, S. J. 2003 Localization in elastic and inelastic scattering. *Ultramicroscopy* **96**, 313–322. (doi:10.1016/S0304-3991(03)00096-2)

Lupini, A. R. *et al.* 2007 Scanning transmission electron microscopy. In *Nanocharacterization* (eds A. I. Kirkland & J. L. Hutchison), pp. 28–65. London, UK: The Royal Society of Chemistry.

Marinopoulos, A. G., van Benthem, K., Rashkeev, S. N., Pennycook, S. J. & Pantelides, S. T. 2008 Impurity segregation and ordering in $Si/SiO_2/HfO_2$ structures. *Phys. Rev. B* **77**, 195317. (doi:10.1103/PhysRevB.77.195317)

Molina, S. I. *et al.* 2006 Determination of the strain generated in InAs/InP quantum wires: prediction of nucleation sites. *Nanotechnology* **17**, 5652–5658. (doi:10.1088/0957-4484/17/22/020)

Molina, S. I. *et al.* 2007 Direct imaging of quantum wires nucleated at diatomic steps. *Appl. Phys. Lett.* **91**, 143112. (doi:10.1063/1.2790483)

Muller, D. A., Kourkoutis, L. F., Murfitt, M., Song, J. H., Hwang, H. Y., Silcox, J., Dellby, N. & Krivanek, O. L. 2008 Atomic-scale chemical imaging of composition and bonding by aberration-corrected microscopy. *Science* **319**, 1073–1076. (doi:10.1126/science.1148820)

Müller, H., Uhlemann, S., Hartel, P. & Haider, M. 2006 Advancing the hexapole C_s-corrector for the scanning transmission electron microscope. *Microsc. Microanal.* **12**, 442–455. (doi:10.1017/S1431927606060600)

Nellist, P. D. & Pennycook, S. J. 1996 Direct imaging of the atomic configuration of ultradispersed catalysts. *Science* **274**, 413–415. (doi:10.1126/science.274.5286.413)

Nellist, P. D. & Pennycook, S. J. 1999 Incoherent imaging using dynamically scattered coherent electrons. *Ultramicroscopy* **78**, 111–124. (doi:10.1016/S0304-3991(99)0017-0)

Nellist, P. D. *et al.* 2004 Direct sub-angstrom imaging of a crystal lattice. *Science* **305**, 1741–1741. (doi:10.1126/science.1100965)

Nellist, P. D., Behan, G., Kirkland, A. I. & Hetherington, C. J. D. 2006 Confocal operation of a transmission electron microscope with two aberration correctors. *Appl. Phys. Lett.* **89**, 124105. (doi:10.1063/1.2356699)

Nellist, P. D., Cosgriff, E. C., Behan, G. & Kirkland, A. I. 2008 Imaging modes for scanning confocal electron microscopy in a double aberration-corrected transmission electron microscope. *Microsc. Microanal.* **14**, 82–88. (doi:10.1017/s1431927608080057)

Oh, S. H. *et al.* 2008 Point defect configurations of supersaturated Au atoms inside Si nanowires. *Nano Lett.* **8**, 1016–1019. (doi:10.1021/nl072670)

Oxley, M. P. & Pennycook, S. J. 2008 Image simulation for electron energy loss spectroscopy. *Micron* **39**, 676–684. (doi:10.1016/j.micron.2007.10.020)

Oxley, M. P., Varela, M., Pennycook, T. J., van Benthem, K., Findlay, S. D., D'Alfonso, A. J., Allen, L. J. & Pennycook, S. J. 2007 Interpreting atomic-resolution spectroscopic images. *Phys. Rev. B* **76**, 064303. (doi:10.1103/PhysRevB.76.064303)

Peng, Y. P., Nellist, P. D. & Pennycook, S. J. 2004 HAADF-STEM imaging with sub-angstrom probes: a full Bloch wave analysis. *J. Electron Microsc.* **53**, 257–266. (doi:10.1093/jmicro/53.3.257)

Peng, Y., Oxley, M. P., Lupini, A. R., Chisholm, M. F. & Pennycook, S. J. 2008 Spatial resolution and information transfer in scanning transmission electron microscopy. *Microsc. Microanal.* **14**, 36–47. (doi:10.1017/S1431927608080161)

Pennycook, S. J. 1988 Delocalization corrections for electron channeling analysis. *Ultramicroscopy* **26**, 239–248. (doi:10.1016/0304-3991(88)90397-X)

Pennycook, S. J. 2006 Microscopy: transmission electron microscopy. In *Encyclopedia of condensed matter physics* (eds F. Bassani, J. Liedl & P. Wyder), pp. 240–247. Kidlington, Oxford: Elsevier Science Ltd.

Pennycook, S. J. 2008 Investigating the optical properties of dislocations by scanning transmission electron microscopy. *Scanning* **30**, 287–298. (doi:10.1002/sca.20114)

Pennycook, S. J. & Jesson, D. E. 1990 High-resolution incoherent imaging of crystals. *Phys. Rev. Lett.* **64**, 938–941. (doi:10.1103/PhysRevLett.64.938)

Pennycook, S. J. & Jesson, D. E. 1991 High-resolution Z-contrast imaging of crystals. *Ultramicroscopy* **37**, 14–38. (doi:10.1016/0304-3991(91)90004-P)

Pennycook, S. J., Varela, M., Hetherington, C. J. D. & Kirkland, A. I. 2006 Materials advances through aberration-corrected electron microscopy. *MRS Bull.* **31**, 36–43.

Pennycook, S. J., Lupini, A. R., Varela, M., Borisevich, A. Y., Peng, Y., Oxley, M. P., van Benthem, K. & Chisholm, M. F. 2007 Scanning transmission electron microscopy for nanostructure characterization. In *Scanning microscopy for nanotechnology: techniques and applications* (eds W. Zhou & Z. L. Wang), pp. 152–191. New York, NY: Springer.

Pennycook, S. J., Chisholm, M. F., Lupini, A. R., Varela, M., van Benthem, K., Borisevich, A. Y., Oxley, M. P., Luo, W. & Pantelides, S. T. 2008*a* Materials applications of aberration-corrected STEM. In *Aberration-corrected electron microscopy* (ed. P. W. Hawkes), pp. 327–384. Oxford, UK: Academic Press.

Pennycook, S. J. *et al.* 2008*b* Scanning transmission electron microscopy of nanostructures. In *Frontiers in nanoscience and nanotechnology* (ed. A. V. Narlikar), pp. 273–286. Oxford, UK: Oxford University Press.

Pennycook, S. J., Varela, M., Lupini, A. R., Oxley, M. P. & Chisholm, M. F. 2009 Atomic-resolution spectroscopic imaging: past, present and future. *J. Electron Microsc.* **58**, 87–97. (doi:10.1093/jmicro/dfn030)

Progl, C. L., Parish, C. M., Vitarelli, J. P. & Russell, P. E. 2008 Analysis of V defects in GaN-based light emitting diodes by scanning transmission electron microscopy and electron beam induced current. *Appl. Phys. Lett.* **92**, 242103. (doi:10.1063/1.2945232)

Rashkeev, S. N., Lupini, A. R., Overbury, S. H., Pennycook, S. J. & Pantelides, S. T. 2007 Role of the nanoscale in catalytic CO oxidation by supported Au and Pt nanostructures. *Phys. Rev. B* **76**, 035438. (doi:10.1103/physRevB.76.035438)

Ritchie, R. H. & Howie, A. 1988 Inelastic-scattering probabilities in scanning-transmission electron-microscopy. *Phil. Mag. A* **58**, 753–767. (doi:10.1080/01418618808209951)

Roberts, K. G., Varela, M., Rashkeev, S., Pantelides, S. T., Pennycook, S. J. & Krishnan, K. M. 2008 Defect-mediated ferromagnetism in insulating Co-doped anatase TiO_2 thin films. *Phys. Rev. B* **78**, 014409. (doi:10.1103/PhysRevB.78.014409)

Rose, H. 1976 Image formation by inelastically scattered electrons in electron microscopy. *Optik* **45**, 139–158, 187–208.

Sawada, H. *et al.* 2007 Achieving 63 pm resolution in scanning transmission electron microscope with spherical aberration corrector. *Jpn. J. Appl. Phys.* **46**, L568–L570. (doi:10.1143/jjap.46.l568)

Sohlberg, K., Pennycook, S. J. & Pantelides, S. T. 1999 Explanation of the observed dearth of three-coordinated Al on gamma-alumina surfaces. *J. Am. Chem. Soc.* **121**, 10 999–11 001. (doi:10.1021/ja9926358)

Sohlberg, K., Rashkeev, S., Borisevich, A. Y., Pennycook, S. J. & Pantelides, S. T. 2004 Origin of anomalous Pt–Pt distances in the Pt/alumina catalytic system. *Chemphyschem* **5**, 1893–1897. (doi:10.1002/cphc.200400212)

Sohlberg, K., Zhuo, S. P., Nellist, P., Peng, Y. P. & Pennycook, S. 2008 Evidence of high-pressure rhodium sesquioxide in the rhodium/gamma-alumina catalytic system. *J. Phys. Chem. C* **112**, 11 831–11 834. (doi:10.1021/jp801089j)

Steele, B. C. H. & Heinzel, A. 2001 Materials for fuel-cell technologies. *Nature* **414**, 345–352. (doi:10.1038/35104620)

Valden, M., Lai, X. & Goodman, D. W. 1998 Onset of catalytic activity of gold clusters on titania with the appearance of nonmetallic properties. *Science* **281**, 1647–1650. (doi:10.1126/science.281.5383.1647)

van Benthem, K. *et al.* 2005 Three-dimensional imaging of individual hafnium atoms inside a semiconductor device. *Appl. Phys. Lett.* **87**, 034104. (doi:10.1063/1.1991989)

van Benthem, K., Lupini, A. R., Oxley, M. P., Findlay, S. D., Allen, L. J. & Pennycook, S. J. 2006 Three-dimensional ADF imaging of individual atoms by through-focal series scanning transmission electron microscopy. *Ultramicroscopy* **106**, 1062–1068. (doi:10.1016/j.ultramic.2006.04.020)

Varela, M. *et al.* 2004 Spectroscopic imaging of single atoms within a bulk solid. *Phys. Rev. Lett.* **92**, 095502. (doi:10.1103/PhysRevLett.92.095502)

Varela, M., Lupini, A. R., van Benthem, K., Borisevich, A., Chisholm, M. F., Shibata, N., Abe, E. & Pennycook, S. J. 2005 Materials characterization in the aberration-corrected

scanning transmission electron microscope. *Annu. Rev. Mater. Res.* **35**, 539–569. (doi:10.1146/annurev.matsci.35.102103.090513)

Voyles, P. M., Muller, D. A., Grazul, J. L., Citrin, P. H. & Gossmann, H. J. L. 2002 Atomic-scale imaging of individual dopant atoms and clusters in highly *n*-type bulk Si. *Nature* **416**, 826–829. (doi:10.1038/416826a)

Wang, S. W., Borisevich, A. Y., Rashkeev, S. N., Glazoff, M. V., Sohlberg, K., Pennycook, S. J. & Pantelides, S. T. 2004 Dopants adsorbed as single atoms prevent degradation of catalysts. *Nat. Mater.* **3**, 274. (doi:10.1038/nmat1100)

Yoon, B., Hakkinen, H. & Landman, U. 2003 Interaction of O_2 with gold clusters: molecular and dissociative adsorption. *J. Phys. Chem. A* **107**, 4066–4071. (doi:10.1021/jp027596s)

Zeitler, E. & Thomson, M. G. R. 1970 Scanning transmission electron microscopy. 1. *Optik* **31**, 258–280.

Zhou, R.-S. & Snyder, R. L. 1991 Structures and transformation mechanisms of the η, γ and θ transition aluminas. *Acta Cryst.* **B47**, 617. (doi:10.1107/S0108768191002719)

Zhu, H. G., Pan, Z. W., Chen, B., Lee, B., Mahurin, S. M., Overbury, S. H. & Dai, S. 2004 Synthesis of ordered mixed titania and silica mesostructured monoliths for gold catalysts. *J. Phys. Chem. B* **108**, 20 038–20 044. (doi:10.1021/yp475250)